NEUROSCIENCE

The inner core enables transient touch detection in the Pacinian corpuscle

Luke H. Ziolkowski[1]†, Yury A. Nikolaev[1]†, Akitoshi Chikamoto[1], Mai Oda[1], Viktor V. Feketa[1,2], David Monedero-Alonso[1], Serafima A. Ardasheva[1], Samuel S. Bae[1], C. Shan Xu[1], Song Pang[3], Elena O. Gracheva[1,2,4,5]*, Sviatoslav N. Bagriantsev[1]*

Pacinian corpuscles detect transient touch and vibration in vertebrates. Corpuscles are composed of a mechanoreceptor afferent surrounded by lamellar Schwann cells (LSCs), enclosed by a multilayered outer core. The spatial arrangement of these components and their contribution to sensory tuning are unclear. We report the three-dimensional architecture of the Pacinian corpuscle and reveal the role of its cellular components in touch detection. In the prevailing model, the outer core acts as a mechanical filter that limits static and low-frequency stimuli from reaching the afferent terminal—the presumed sole site of touch detection. We show that the outer core is dispensable for the sensory tuning to transient touch and vibration; instead, these properties arise from the inner core. By acting as additional touch sensors, LSCs potentiate mechanosensitivity of the terminal, which detects touch via fast inactivating ion channels. Thus, functional tuning of the Pacinian corpuscle is enabled by an interplay between mechanosensitive LSCs and the afferent terminal in the inner core.

INTRODUCTION

Pacinian corpuscles detect transient touch and high-frequency vibration due to their ability to respond only to dynamic but not static stimuli (a process called rapid adaptation) and exhibit increased sensitivity to high-frequency vibration (high-pass frequency filtering) (1–9). Despite the variation in size and anatomical location, Pacinian corpuscles from different species exhibit comparable overall architecture and sensory properties (3, 10–16), suggesting a unifying mechanism of touch detection. The exterior capsule (the outer core) of Pacinian corpuscles is formed by layers of outer core lamellar cells (OCLCs), which create a diffusion-restricting barrier around the inner core composed of lamellar Schwann cells (LSCs) surrounding the mechanoreceptor afferent terminal (11). The accepted view is that the multilayered structure of the outer core together with turgor pressure in the inner cavity form a mechanical filter restricting static and low-frequency stimuli from reaching the terminal, thus enabling rapid adaptation and frequency tuning (17–19). However, experimental and modeling data show that these properties remain largely invariant regardless of the number of outer core layers (20), calling for a reexamination of the role of the outer core in shaping corpuscle function.

In the inner core, each LSC sprouts numerous semiconcentric processes, known as inner core lamellae, around the afferent terminal. Although the terminal is thought to be the sole site of touch detection in Pacinian corpuscles, LSCs were hypothesized to play structural, developmental, supportive, and trophic roles (17, 21–25), but whether LSCs actively participate in touch detection is unknown. To our knowledge, patch-clamp recordings from LSCs or

the terminal have not been reported in any species and the process of mechanoelectric conversion in Pacinian corpuscles remains unexplored. Understanding the mechanism of Pacinian corpuscle function also requires establishing the spatial arrangement of its cellular components, which is currently missing except for the structure of the afferent terminal (15). In this study, we combined structural and functional studies to determine the high-resolution three-dimensional (3D) architecture of a Pacinian corpuscle and reveal the contribution of its cellular components to touch detection. We propose a model in which the functional tuning of Pacinian corpuscles toward the detection of transient touch in vibration is mediated by an interplay between mechanosensitive LSCs and the afferent terminal in the inner core.

RESULTS

3D architecture of the Pacinian corpuscle

We used enhanced focused ion beam scanning electron microscopy (eFIB-SEM) to determine the architecture of the Pacinian corpuscle in the bill skin of the late-stage embryonic tactile specialist Mallard duck (3, 26–28) at a voxel size of 8 nm by 8 nm by 8 nm (Fig. 1, A to D, and table S1). The reconstructed corpuscle had an ovoid shape measuring 66 µm along the long axis and a diameter in the widest region of 53 µm (movie S1). Flattened OCLCs form the outer core of the corpuscle (Fig. 1, C to E), creating a diffusion barrier around the inner core (11, 29–31), which resides in the inner cavity surrounded by collagen fibers (fig. S1). The inner core is composed of 12 LSCs, each sprouting thin concentric lamellae, which interleave with the lamellae from neighboring LSCs and envelop a portion of the afferent terminal (Figs. 1, F and G, and 2A and fig. S2). When viewed in a cross section, the 48-µm–long terminal is elliptical, with its long axis aligned with the cleft in the surrounding LSC lamellae (fig. S3). The cytosol of the terminal contains densely packed elongated mitochondria (fig. S4, A and B), clear vesicles, and occasional dense core vesicles, which are more abundant in the ultraterminal bulbous end (fig. S4, C and D). Twenty-nine spike-like protrusions emanate from the opposing sides of the ovoid afferent, facing the cleft in the LSCs

[1]Department of Cellular and Molecular Physiology, Yale University School of Medicine, New Haven, CT 06520, USA. [2]Department of Neuroscience, Yale University School of Medicine, New Haven, CT 06520, USA. [3]FIB-SEM Collaboration Core, Yale University School of Medicine, New Haven, CT 06520, USA. [4]Program in Cellular Neuroscience, Neurodegeneration and Repair, Yale University School of Medicine, New Haven, CT 06520, USA. [5]Kavli Institute for Neuroscience, Yale University School of Medicine, New Haven, CT 06520, USA.
*Corresponding author. Email: elena.gracheva@yale.edu (E.O.G.); slav.bagriantsev@yale.edu (S.N.B.)
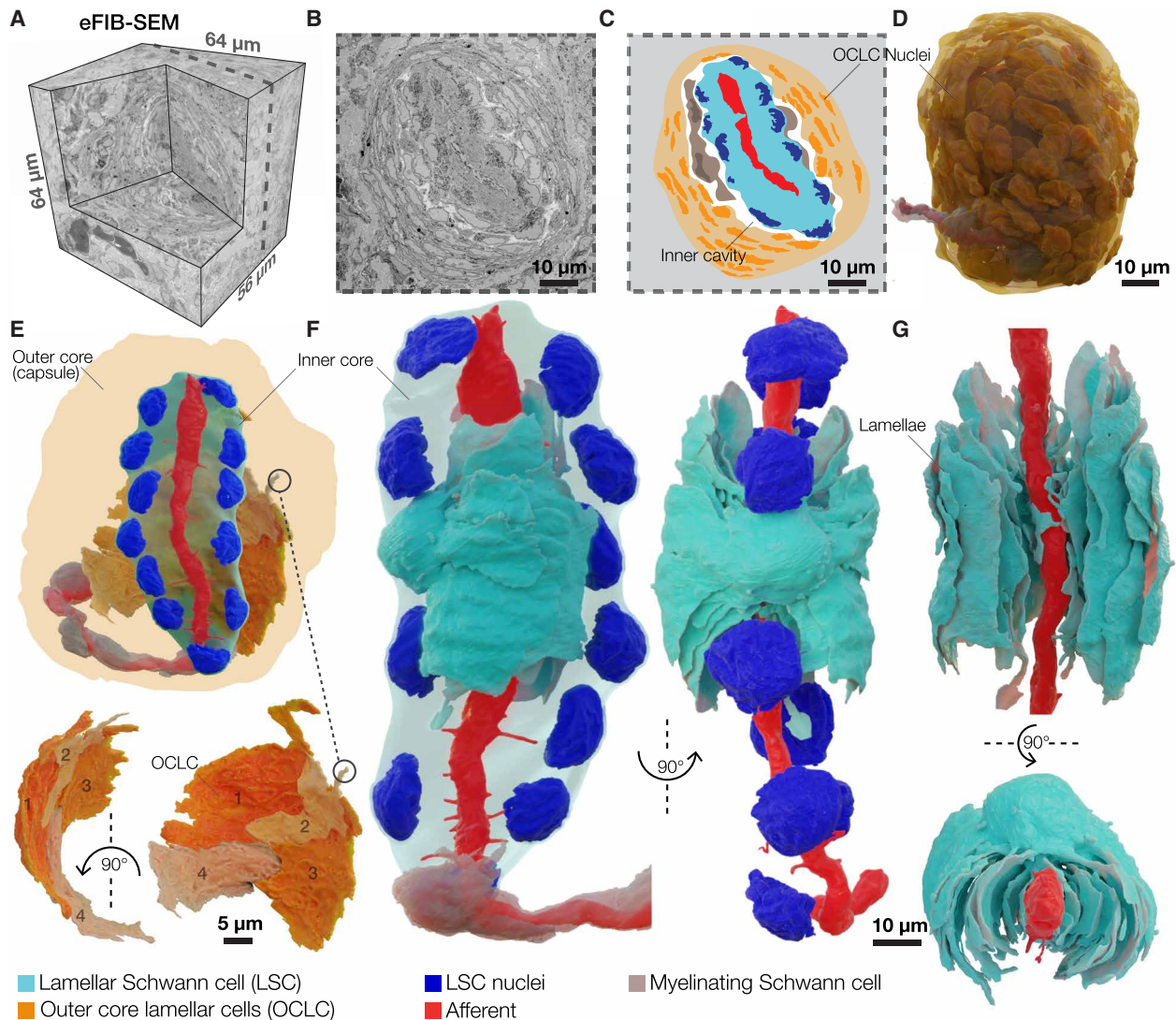†These authors contributed equally to this work.

Fig. 1. 3D architecture of the Pacinian corpuscle. (**A**) 3D volume of duck bill skin dermis obtained by eFIB-SEM with an 8-nm³ resolution. (**B** and **C**) Single eFIB-SEM image (B) and an illustration (C) of a section of an avian Pacinian corpuscle. (**D**) 3D reconstruction of the Pacinian corpuscle. (**E**) 3D reconstruction of the Pacinian corpuscle showing the location of the inner core inside the outer core (top) and 3D reconstruction of four outer core lamellar cells (OCLCs) (bottom). (**F** and **G**) 3D reconstruction of the inner core showing the architecture of the afferent terminal and 1 of 12 LSCs. Different shades of cyan denote lamellae from the same lamellar Schwann cell (LSC).

(Fig. 2, A and B, and fig. S3). The protrusions, which are considered as putative sites of mechanotransduction (*13–15*), reach the lamellae of surrounding LSCs, but the longest protrusions extended to the LSC body (Fig. 2, C and D). We also performed eFIB-SEM imaging of another Pacinian corpuscle, which had similar overall architecture: It contained 17 LSCs (fig. S5, A to C, and table S1) surrounding a 69-μm-long terminal with 55 protrusions (fig. S5, D to F). Using 3D transmission electron microscopy (TEM) tomography, we reconstructed a volume of 1.6 μm by 1.3 μm by 0.15 μm containing LSC lamellae near the terminal of the corpuscle (Fig. 2E). LSC lamellae contained caveolae and formed contacts with adjacent lamellae via gap junctions (fig. S6), adherens junctions, and tethers (Fig. 2F). Notably, numerous adherens junctions and tethers also connected inner core lamellae and afferent terminal membranes, demonstrating tight physical coupling between the Schwann cell and neuronal components of the inner core (Fig. 2F and movie S2).

The outer core is dispensable for firing adaptation and frequency tuning

Pacinian corpuscles in mammals and birds detect transient touch and high-frequency vibration (*1, 3, 6, 7, 11, 16*). They also display rapid adaptation of action potential (AP) firing in the afferent and high-pass frequency filtering. Earlier studies suggested that rapid adaptation and high-pass frequency filtering are enabled by the multilayered structure of the outer core, which acts as a mechanical filter that prevents static and low-frequency stimuli from reaching the afferent terminal. The integrity of the outer core is thus thought to be essential for Pacinian corpuscle function across species (*11, 18, 24, 25, 29, 32*).

To test this hypothesis, we used an ex vivo preparation from late-stage embryonic duck bill skin (*28, 33*). A step mechanical indentation applied onto the corpuscle evoked APs in the afferent during the dynamic, but not the static, phases of the stimulus, i.e.,
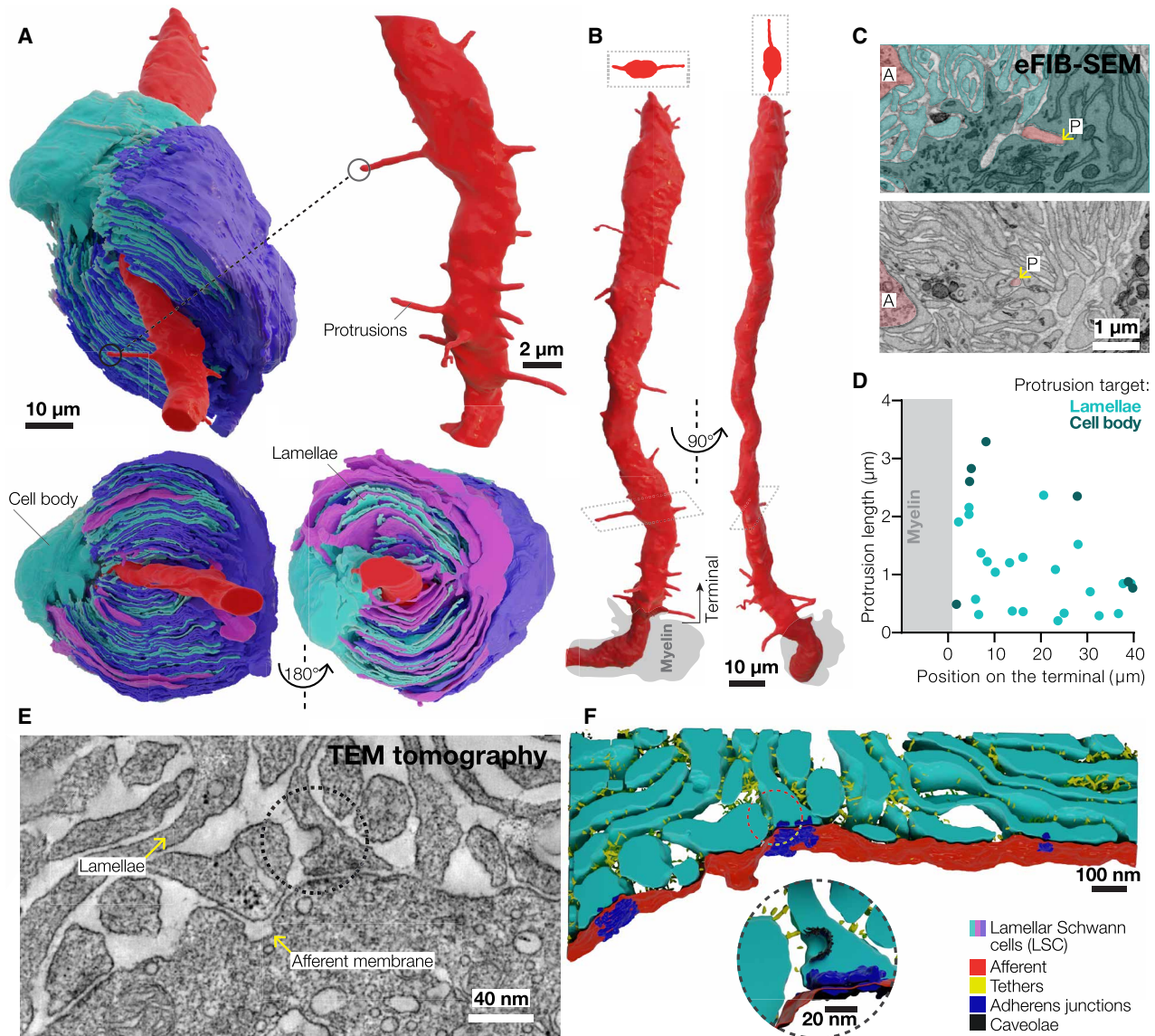
Fig. 2. 3D architecture of lamellar Schwann cells (LSCs) and the afferent terminal in the Pacinian corpuscle. (**A**) 3D reconstruction of a pair of opposing LSCs from the inner core (top panel). The interdigitating lamellae from the LSCs encompass the afferent terminal (bottom panel). (**B**) 3D reconstruction of the afferent terminal with 29 protrusions. Two cross-sectional views are shown at the top of the terminal. (**C**) Pseudocolored eFIB-SEM image showing protrusion tips targeting the LSC body (top panel) and lamellae (bottom panel). A, afferent terminal; P, protrusion tip. (**D**) Localization, length, and terminal target of the afferent protrusions. (**E** and **F**) TEM image (E) and a 3D reconstruction of the lamellae-afferent contact areas.

in the rapidly adapting fashion (Fig. 3, A to D). To test whether the integrity of the outer core and the turgor pressure inside the corpuscle are important for rapid adaptation and frequency filtering, we compared corpuscle function before and after rupturing the outer core via the combination of mechanical disruption and a high-pressure stream of Krebs solution from the patch pipette (Fig. 3E and Materials and Methods). Notably, this procedure failed to affect the rapid adaptation and high-pass frequency filtering as the afferent continued to fire only during the dynamic ON and OFF phases with unchanged activation threshold (Fig. 3F) and exhibited a characteristic decrease in the activation threshold upon increasing stimulation frequency (Fig. 3, G and H). Thus, our data show that, contrary to the accepted model, the integrity of the

outer core and the turgor pressure are dispensable for rapid adaptation and frequency tuning.

To test the hypothesis that the outer core influences mechanotransduction in the afferent terminal (*18*, *24*, *25*), we performed patch-clamp recordings from the terminal at the nonmyelinated heminode inside the corpuscle (Fig. 4A). The gap junction–permeable fluorescent dye Lucifer yellow injected into the terminal via the patch electrode remained confined within its bounds, confirming intracellular access and showing the absence of the dye-permeable gap junctions between the afferent and surrounding cells (Fig. 4B). The terminal had a resting membrane potential of -64.28 ± 1.52 mV, whole-cell capacitance of 11.36 ± 2.04 pF, and input resistance of 238.6 ± 85.96 megohms (means $\pm$ SEM, $n = 5$). Mechanical
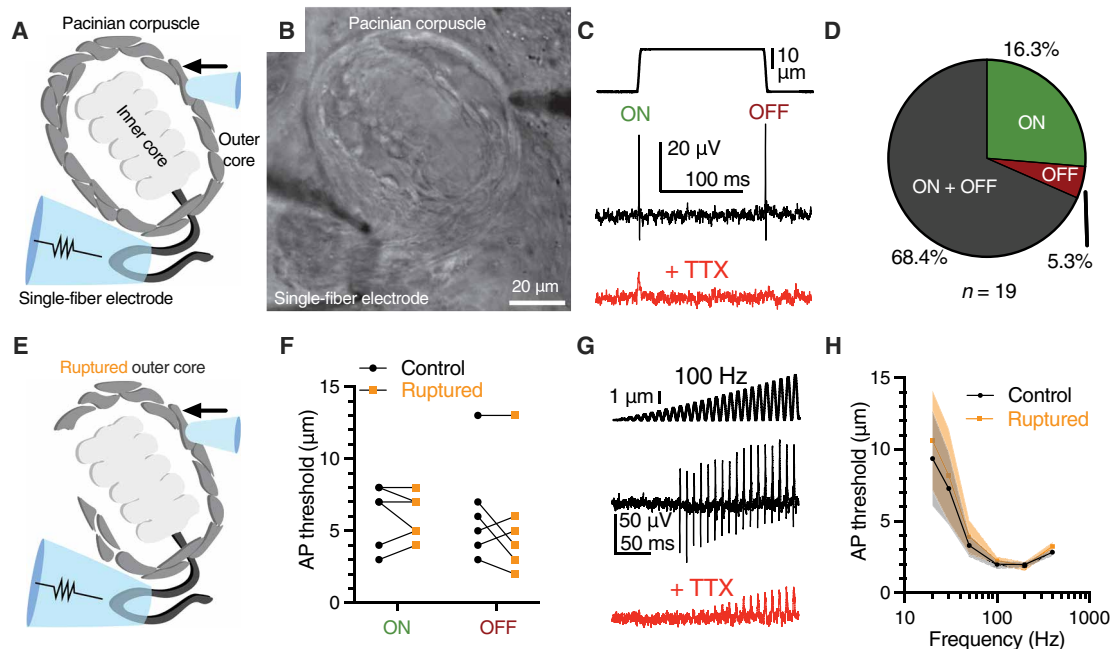
Fig. 3. Outer core integrity is dispensable for rapid adaptation and frequency tuning of the Pacinian corpuscle. (**A** and **B**) Illustration (A) and bright-field image (B) of the setup for single-fiber recording from the Pacinian afferent. (**C**) Mechanical step stimulus (top) and a representative single-fiber recording from the Pacinian afferent (middle) with 1 μM tetrodotoxin (TTX) added to block APs (bottom). (**D**) Proportion of Pacinian mechanoreceptors that fire AP in the dynamic onset (ON), offset (OFF), or both ON and OFF phases. (**E**) Illustration of a Pacinian corpuscle with the outer layers of outer core lamellar cells (OCLCs) ruptured. (**F**) Threshold comparison of the ON and OFF responses using the protocol in (C). Connected symbols represent paired observations from the same corpuscle. No difference between the intact (control) and ruptured outer core conditions was detected [two-way repeated measures analysis of variance (ANOVA), $P = 0.2865$]. (**G**) A 100-Hz sinusoidal-ramp mechanical stimulus applied to corpuscles (top) and an exemplar single-fiber response (middle) with 1 μM TTX added to block APs (bottom). (**H**) Population tuning curve of Pacinian afferents using a sinusoidal-ramp protocol (G) to measure the threshold for AP firing at a range of frequencies (means ± SEM, $n = 7$ corpuscles). No difference between the intact (control) and ruptured outer core conditions was detected (two-way repeated measures ANOVA, $P = 0.1163$).

stimulation applied through the outer core while current-clamping the afferent terminal elicited APs in the terminal, whereas in the voltage-clamp mode, it evoked mechanically activated (MA) currents during the ON and OFF dynamic phases (Fig. 4, C and D), in agreement with the rapidly adapting firing recorded in the afferent outside the corpuscle (Fig. 3C). To directly test whether the outer core influences afferent terminal mechanotransduction, we decapsulated the corpuscle by removing the outer core and stimulated the inner core directly (Fig. 4, E and F). Notably, and in agreement with our experiments above, the MA current in decapsulated corpuscles still occurred only during the dynamic phases of the stimulus (Fig. 4G) and retained equally fast kinetics of activation and inactivation (Fig. 4, H and I). We observed an increase in MA current amplitude after decapsulation (Fig. 4, J and K) and a small decrease in the threshold of activation for both ON and OFF responses (Fig. 4L). Thus, our results support the idea that, although the outer core may present a physical layer that attenuates the threshold of stimulus detection, it does not influence the kinetics of mechanotransduction in the terminal.

Our results are at variance with the earlier studies of receptor potential decay in a Pacinian afferent, which indirectly suggested that MA currents in the terminal have slow kinetics of inactivation and only appear fast due to the presence of the mechanical filter formed by the outer core (*18, 24, 25*). Searching for a cause for this apparent contradiction, we noticed that decapsulation eventually leads to a visible deterioration of the afferent terminal, and 10 min after decapsulation, the "leak" current through the terminal membrane increases, and the MA current begins to show slow inactivation kinetics (fig. S7, A to D). Slower inactivation rates were correlated with larger leak current at the holding potential of −60 mV (fig. S7E), demonstrating that the apparent prolongation of MA current decay is observed only in deteriorating afferent terminals.

Next, we tested whether the outer core is required for high-pass frequency filtering by recording the discharge of the Pacinian afferent in the same corpuscle before and after decapsulation and found that direct stimulation of the inner core failed to affect frequency tuning (Fig. 4M). Together, our data show that, although the outer core likely serves a protective role by providing the optimal environment for the inner core, it is not necessary for rapid adaptation of the afferent discharge, fast inactivation of MA current, or frequency tuning. Instead, these key functions of Pacinian corpuscles originate from the inner core.

Inner core LSCs are touch sensors

Next, we investigated the electrophysiological properties of LSCs by patch-clamp, which, to our knowledge, have not been studied in any species. We found that Lucifer yellow injected into a single LSC via the recording electrode diffused among all LSCs but did not spread into the afferent or other cells (Fig. 5, A and B). Patch-clamp measurements from LSCs revealed a resting membrane potential of −73.01 ± 1.664 mV (means ± SEM, $n = 20$). Consistent with the spread of Lucifer yellow across all LSCs, RNA sequencing of
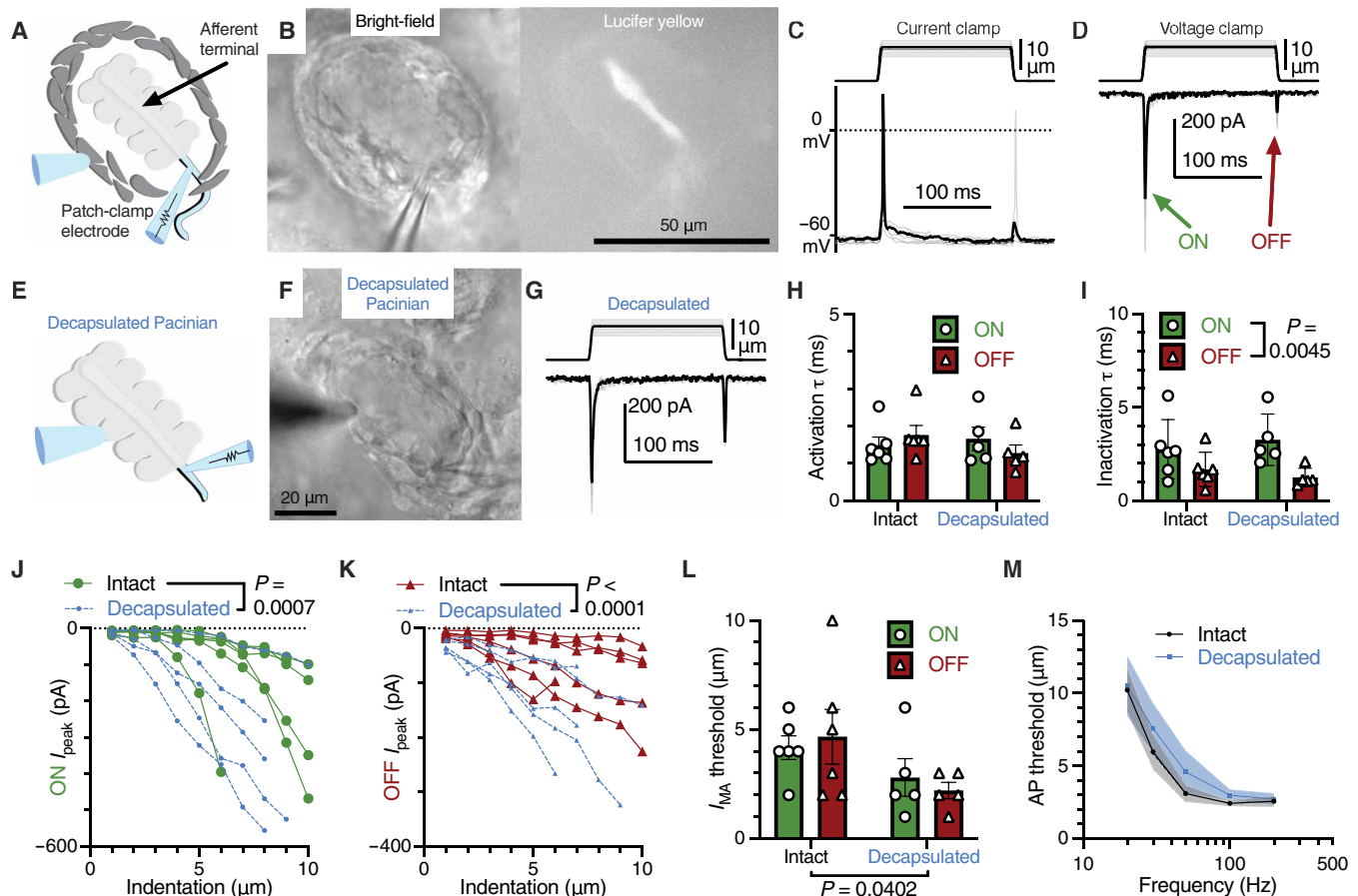
Fig. 4. Rapid adaptation and frequency tuning of the Pacinian terminal is independent of the outer core. (**A**) Illustration of the approach for patch-clamp recording from the Pacinian afferent terminal. (**B**) Bright-field (left) and fluorescent (right) images of a Pacinian corpuscle with the Lucifer yellow–filled electrode in the patch-clamp configuration in contact with the afferent terminal. (**C**) Recordings with the mechanical step stimulus applied with a glass probe (top) and exemplar voltage responses and APs in the terminal in current-clamp mode (bottom). (**D**) Mechanical stimulus (top) and representative MA current responses in the terminal voltage clamped at −60 mV (bottom). (**E**) Illustration of patch-clamp recordings of the terminal of a decapsulated Pacinian corpuscle. (**F**) Bright-field image of a decapsulated Pacinian corpuscle. (**G**) Mechanical stimulus (top) and exemplar MA current responses in a decapsulated Pacinian terminal (bottom). (**H** and **I**) Quantification of the kinetics of MA current activation (H) and inactivation (I) during the ON and OFF phases in intact and decapsulated corpuscles. Symbols denote values from individual corpuscles (means ± SEM). Decapsulation had no significant effect on the kinetics of MA current activation ($P = 0.5409$) or inactivation ($P = 0.9418$). Statistics: two-way ANOVA. (**J** and **K**) Quantification of the amplitude of peak MA currents in the afferent terminal in the ON (J) and OFF (K) phases in relation to the indentation depth of the probe. Each line represents data from one cell. Statistics: two-way ANOVA. (**L**) Comparison of the current response threshold of the ON and OFF phases between terminals of intact and decapsulated corpuscles. Symbols denote values from individual corpuscles (means ± SEM). Statistics: two-way ANOVA. (**M**) Population tuning curves of intact and decapsulated corpuscles measured via single-fiber recording from the afferent (means ± SEM, $n = 6$ corpuscles). Decapsulation had no significant effect (two-way repeated measures ANOVA, $P = 0.3842$).

individual inner cores revealed the presence of gap junction transcripts (fig. S8 and data S1). The pan-gap junction blocker carbenoxolone (CBX) reduced the whole-cell capacitance of the inner core 12-fold and doubled the input resistance (Fig. 5, C to E), confirming functional gap junction coupling between LSCs. Dual patch-clamp recordings showed a coupling coefficient between two adjacent LSCs in response to current injection at 0.52 ± 0.08 (means ± SEM, $n = 6$), and this value diminished in the presence of CBX (Fig. 5, F to H). The coupling coefficient decreased with larger current injections (fig. S9). Thus, LSCs form a gap junction–coupled syncytium, which permits the passage of small molecules but allows for only limited electrical coupling between LSCs.

Our RNA sequencing of Pacinian inner cores revealed expression of various types of mechanically gated ion channels and

associated proteins (*34–36*) and voltage-gated ion channels (fig. S8B), suggesting that LSCs could be mechanosensitive and excitable. Indeed, LSCs responded to mechanical stimulation with robust noninactivating MA current, which increased in magnitude with larger indentation depths (Fig. 6, A and B) and displayed a linear voltage dependence with a reversal potential of 16.40 mV (Fig. 6C), indicative of poor ionic selectivity. This result strongly suggests that LSCs express mechanically gated ion channels, which are engaged during corpuscle deformation either directly or with the help of nearby cellular elements, such as adjacent protrusions from the afferent terminal. We also found that LSCs express voltage-gated potassium channels, as well as voltage-activated sodium and/or calcium channels (fig. S10, A and B). The voltage dependence of activation of the excitatory conductances appear
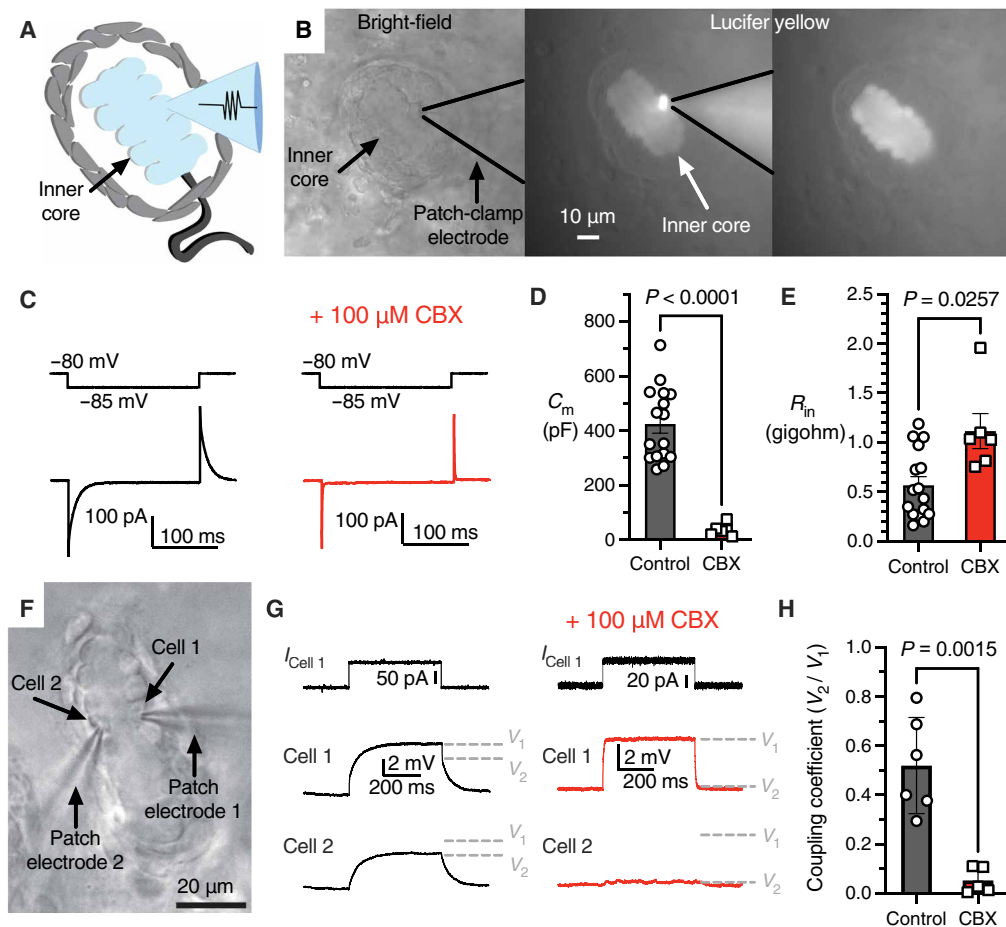
Fig. 5. Lamellar Schwann cells (LSCs) form a gap junction–coupled syncytium. (**A**) Illustration of interconnected, patch-clamped inner core LSCs. (**B**) Bright-field image of a patch-clamped LSC (left), fluorescence of Lucifer yellow in the patched inner core (middle), and fluorescence in the inner core after the patch electrode is removed (right). (**C**) Voltage step applied to the patched LSC (top) and the example current responses (bottom) with normal intracellular solution or including the gap junction blocker CBX (right). (**D** and **E**) Membrane capacitance (D) and input resistance (E) with and without CBX. Symbols denote recordings from individual corpuscles (means ± SEM). Statistics: Welch's t test. (**F**) Bright-field image of simultaneous patch-clamp recordings from two LSCs. (**G**) Simultaneous recordings from adjacent LSCs (Cell 1 and Cell 2). A current injection stimulus applied to Cell 1 in the recording setup in (F) (top), an example voltage response in Cell 1 (middle), and an example voltage response in the connected Cell 2 (bottom), with normal intracellular solution or including CBX. V_1 and V_2 denote voltage levels induced in Cell 1 and Cell 2, respectively. (**H**) Coupling coefficient between two cells under control conditions versus with CBX. Symbols denote recordings from individual corpuscles (means ± SEM). Statistics: Welch's t test.

stretched toward positive potentials (fig. S10C) in comparison with known voltage-gated sodium and potassium channels in vitro and in native cells (*37*), suggesting that many of these channels are expressed in the long lamellar processes of LSCs, and the recorded right-shifted voltage dependence likely reflects voltage drop produced by the high electrical resistance of these structures.

To test whether activation of an LSC can modulate mechanosensitivity of the afferent terminal, we performed voltage-clamp recordings in the terminal paired with simultaneous activation of an LSC (Fig. 6D). We detected a depolarizing inward current in the terminal in response to activation of an LSC with current injection (Fig. 6E). In contrast, activation of an LSC failed to induce current in an adjacent OCLC, demonstrating that the functional coupling was specifically between the LSC and the mechanoreceptor terminal (Fig. 6F). Consistently, in current-clamp mode, the afferent terminal depolarized upon LSC activation, and the

depolarization increased with larger current injection into the LSC (Fig. 6, G and H).

Having established that LSCs can influence the excitatory status of the afferent, we hypothesized that LSC-induced depolarization of the afferent terminal should lower the threshold of mechanical stimulation required for the mechanoreceptor to generate an AP. We found that activation of an LSC by current injection triggered AP firing in the afferent in response to a subthreshold mechanical stimulus (Fig. 6, I and J) and led to an overall reduction in the threshold required for activation of the afferent by mechanical force (Fig. 6K). In agreement with our data, the accompanying study shows that optogenetic activation of LSCs in mouse Pacinian corpuscles also decreases the threshold of mechanical activation (*38*). Together, our works establish an evolutionarily conserved role of LSCs as active mechanosensory elements within Pacinian corpuscles that potentiate sensitivity of the afferent terminal to mechanical touch.
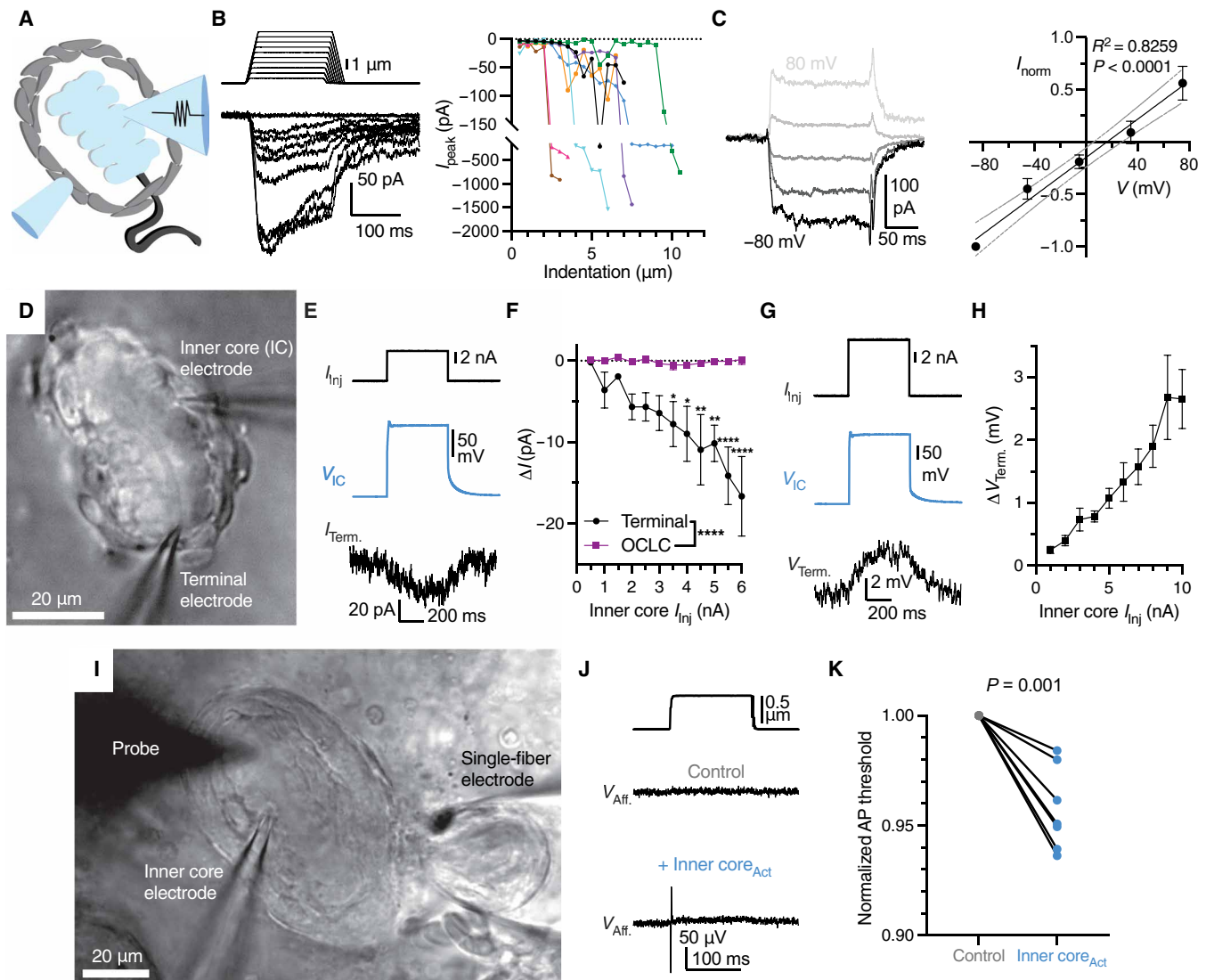
Fig. 6. Activation of mechanosensitive lamellar Schwann cells (LSCs) reduces the mechanosensitivity threshold of the Pacinian corpuscle. (**A**) Illustration of a patch-clamped LSC with a probe for mechanical stimulation. (**B**) Mechanical step stimuli (top left), example voltage-clamp recordings (bottom left) from an LSC held at −80 mV, and quantification of peak MA current (right). Lines connect data from individual LSCs. (**C**) Example MA current responses in an LSC at different voltages and the current-voltage relationship of MA current (means ± SEM, $n = 6$ LSCs). (**D**) Bright-field image of paired patch-clamp recordings from one LSC and the afferent terminal of the same corpuscle. (**E**) Exemplar traces showing current injection stimulus applied to an LSC (top), voltage response of the LSC (middle), and current response of the afferent terminal voltage clamped at −60 mV (bottom). (**F**) Quantification of current responses in the afferent terminal and an outer core lamellar cell (OCLC) upon current injection into an LSC (means ± SEM from four afferent terminal and four OCLCs). Statistics: two-way ANOVA with Holm-Šídák post hoc tests (*$P < 0.05$; **$P < 0.01$; ****$P < 0.0001$). (**G**) Exemplar traces showing current injection into an LSC (top), voltage response of the LSC (middle), and voltage response of the current-clamped afferent terminal (bottom). (**H**) Quantification of voltage response in the afferent terminal upon current injection into an LSC (means ± SEM, $n = 7$). (**I**) Bright-field image of paired patch-clamp recordings from one LSC and single-fiber recording from the afferent during mechanical stimulation with a probe. (**J**) Mechanical stimulus (top) and single-fiber recordings of the Pacinian afferent in the absence (middle) or presence (bottom) of LSC–inner core activation via 6-nA current injection. (**K**) Quantification of the effect of LSC activation by depolarizing current (6 nA) on the threshold of mechanical activation recorded in the afferent. Lines connect data from paired recordings. Statistics: one sample t test.

DISCUSSION

Our results demonstrate that, contrary to the accepted view, the outer core is dispensable for rapid adaptation and frequency tuning—the main functional properties of Pacinian corpuscles. When the integrity of the outer core is compromised, or when mechanical stimulation is delivered to the inner core directly, the afferent continues to display rapid adaptation and high-pass frequency filtering.

Earlier observations using Pacinian corpuscles from cat mesentery documented that physical removal of most outer core layers converts the timing of mechanically evoked receptor potential decay from fast to slow (*24, 25, 39, 40*). Other studies, however, noted that this only happens upon intense compression, whereas light forces do not affect the process (*41–43*). These observations suggested a model in which the outer core acts as a multilayered mechanical

cushion that prevents static stimuli from reaching the core and enables rapid adaptation of the receptor potential (*11*, *18–20*). Although our experiments demonstrate that direct mechanical stimulation of isolated inner cores produces the same functional outcome as stimulation of the intact corpuscles, they also show that over time, as the afferent terminal deteriorates, the timing of MA current decay becomes noticeably slow, likely due to an increase in the leak current through the afferent membrane. Our observations thus support a model where the outer core provides a protective environment for the inner core components (*29*, *30*) but is dispensable for rapid adaptation and frequency filtering. Instead, these properties are mediated by the inner core.

The 3D structures of inner cores shown here for the avian Pacinian corpuscle and in the accompanying study for its mouse counterpart (*38*) permit a detailed comparison of both structures. In both cases, the inner core is composed of two columns of LSCs, which extend long interdigitating lamellae, encompassing the entire length of the afferent terminal. The afferent terminal contains thin protrusions, which penetrate through inner core lamellae and extend to the periphery. Although the number of protrusions in the avian Pacinian is smaller than in mouse corpuscles, which could be either species-specific or reflect a developmental stage, they share a similar overall appearance and similarly originate from opposite sides of the elliptical terminal. Because protrusions are present in Pacinians from different species (*13–15*), they are a general feature of Pacinian corpuscles. Although the exact function of the protrusions remains to be determined, they were proposed to be the key sites of mechanotransduction in the terminal (*14*) and, in mice, were shown to express the mechanotransducing ion channel Piezo2 (*15*). Another possibility is that the protrusions participate in a mechanical cross-talk with LSCs, influencing their mechanosensitivity.

Because of their structure and location, the individual components of Pacinian corpuscles have been nearly impervious to direct electrophysiological investigations in the skin and internal membranes of mammals. Here, we performed patch-clamp recordings from the afferent terminal of Pacinian corpuscles in late-stage embryonic duck bill skin to reveal biophysical properties of the underlying mechanically gated ion channels. We found that both ON and OFF MA currents exponentially decay with remarkably fast kinetics. Our measured inactivation constant ($\tau_{\mathrm{inact}} = 1$ to 3 ms) is smaller than those previously recorded in mechanoreceptor afferents in the worm *C. elegans* (*44–47*), in Merkel afferents from mouse whiskers (*48*), and in Meissner corpuscle afferents in ducks (*28*). In mammals, afferents innervating Merkel cells and Meissner and Pacinian corpuscles express Piezo2 (*15*, *49–51*), and it appears likely that this protein also contributes to MA current in avian Pacinian afferents (*52*, *53*). Although the MA current in Pacinian afferents inactivates much faster than mouse or duck Piezo2 in vitro ($\tau_{\mathrm{inact}} \approx 8$ to 10 ms) (*54*, *55*), Piezo2 inactivation is a variable parameter influenced by cell-specific factors (*34*, *56–65*).

The remarkable architecture of the Pacinian inner core presented here and in the accompanying study (*38*) reveals interdigitating crescent-shaped lamellae formed by LSCs that envelop the afferent terminal. This raises the question of whether and how the lamellae formed by LSCs contribute to corpuscle function. One possibility is that the inner core lamellae perform the "mechanical filter" role previously assigned to the outer core. The sensory Schwann cells in mammalian Meissner corpuscles, which exhibit frequency tuning and rapid adaptation, also sprout lamellae around the afferent terminal

but are devoid of an outer core (*15*). Avian Meissner corpuscles also contain sensory Schwann cells (*33*), which are transcriptionally similar to Pacinian LSCs (fig. S11). Like their mammalian counterparts, avian Meissner corpuscles show rapid adaptation and frequency tuning, but their sensory Schwann cells do not form lamellae around the afferent (*27*). These observations demonstrate that a multilayered structure around the afferent is, in principle, not essential for rapid adaptation or frequency tuning.

We show that mechanically gated ion channels in the Pacinian afferent terminal open during the dynamic phases of mechanical stimulus, causing AP firing, but then quickly close and remain inactivated during the static phase. A recent study showed that the efficiency of Piezo2 activation increases with indentation velocity, suggesting that the channel is more efficiently engaged by high frequency stimulation (*66*). Thus, rapid adaptation and frequency filtering may stem from the biophysical properties of the mechanotransducing ion channels in the terminal. However, the accompanying study demonstrates that frequency filtering is also influenced by the activity of LSCs (*38*). Together, our studies suggest a general model where precise adaptation rates and frequency filtering results from an interplay between mechanosensitive LSCs and the afferent in the Pacinian inner core.

Because activation of an LSC decreases the threshold of mechanical activation of the Pacinian afferent, our data establish LSCs as physiologically relevant touch sensors, which facilitate mechanosensitivity of Pacinian corpuscles. The accompanying study shows that this is also true for mouse Pacinians (*38*), demonstrating that the multicellular mechanism of touch detection is evolutionarily conserved in Pacinian corpuscles. How Pacinian LSCs facilitate mechanosensitivity of the afferent terminal remains an open question. Our observations rule out direct electrical coupling between LSCs and the terminal via gap junctions. The absence of clearly identifiable vesicles in LSCs or synapse-like structures between LSCs and the terminal also argues against, although does not rule out, synapse-like mechanisms as reported for Merkel cell-neurite complexes (*48*, *67*, *68*). It is possible that other mechanisms, such as ephaptic cross-talk between adjacent membranes, or ion channel–based communication, such as those mediating interaction between peripheral glia and mechanoreceptors in worms (*69*, *70*) and between keratinocytes and mechanoreceptors in mice (*71*), are at play. The presence of transcripts encoding the motor protein prestin (*SLC26A5*) in the transcriptome of Pacinian inner cores (data S1) suggests that LSCs may potentially exhibit electromotility upon activation, similar to the mechanism in outer hair cells (*72*). Prominent tethers connecting LSC lamellae with afferent membrane suggest yet another possibility of physical coupling between the lamellae and mechanically gated channels in the terminal (*27*, *47*, *73–75*). It remains to be determined whether any of these mechanisms partake in Pacinian corpuscle function and whether they are present in other mechanoreceptive end organs in vertebrates, which contain sensory Schwann cells (*15*, *27*, *76–78*).

MATERIALS AND METHODS
Animals
Experiments with Mallard duck embryos (*Anas platyrhynchos domesticus*) were approved by and performed in accordance with guidelines of the Institutional Animal Care and Use Committee of Yale University (protocol 11526). Animals used in experiments were

at development stages embryonic day 25 (E25) to E27, between 1 and 3 days before hatching; sex was not determined.

Ex vivo bill skin preparation

Dissection of bill skin was performed as described previously (*27*, *28*). First, the glabrous skin of the bill was shaved off from the embryo and placed into ice-cold L-15 media, where it was trimmed to fit into a recording chamber. For experiments involving single-fiber or patch-clamp recording of the afferent, the bill skin was inverted (with the dermis on top and the epidermis on the bottom) in the recording chamber in Krebs solution containing 117 mM NaCl, 3.5 mM KCl, 2.5 mM CaCl$_2$, 1.2 mM MgCl$_2$, 1.2 mM NaH$_2$PO$_4$, 25 mM NaHCO$_3$, and 11 mM glucose, saturated with 95% O$_2$ and 5% CO$_2$ (pH 7.3 to 7.4), at room temperature (22° to 23°C). The bill skin was treated with collagenase P (2 mg/ml; Roche) in Krebs solution for 5 min and then washed with fresh Krebs solution. Bill skin preparations used for solely lamellar cell patch-clamp recording were placed into Ringer solution containing 140 mM NaCl, 5 mM KCl, 10 mM Hepes, 2.5 mM CaCl$_2$, 1 mM MgCl$_2$, and 10 mM glucose at room temperature. The epidermis was carefully removed from the dermis, which was treated with collagenase P (2 mg/ml) in Ringer solution for 5 min and then washed with fresh Ringer. Corpuscles in the dermis were visualized on an Olympus BX51WI upright microscope with an ORCA-Flash 4.0 LT camera (Hamamatsu).

Electrophysiology
Single-fiber electrophysiology from individual Pacinian afferents

Recordings from single afferent fibers of avian Pacinian corpuscles (historically known as Herbst corpuscles) were acquired at room temperature in Krebs solution, using a MultiClamp 700B amplifier and Digidata 1550A digitizer (Molecular Devices). Single-fiber recording pipettes were created from borosilicate glass capillaries with an outer diameter of 1.5 mm, inner diameter of 1.17 mm, and wall thickness of 0.17 mm and without filament (Warner Instruments model GC150T-7.5). Pipettes were pulled using a P-1000 micropipette puller (Sutter Instruments) to create tip diameters of 5 to 30 µm and then filled with Krebs solution. Pipettes were placed on a CV-7B headstage connected to a High-Speed Pressure Clamp (ALA Scientific Instruments). Single corpuscles and connected afferents within the same field of view were identified under a 40X objective lens. The recording pipette was placed next to the afferent, and negative pressure was applied until a large section (~5 µm) of the afferent was sucked into the pipette. The extracellular afferent voltage was recorded in current-clamp mode, sampled at 20 kHz, and low-pass filtered at 1 kHz in Clampex 10.7 (Molecular Devices). A suprathreshold mechanical step stimulus was applied to the connected corpuscle to confirm the presence of mechanically induced APs in the afferent fiber. Fresh Krebs solution was regularly perfused onto the preparation between recordings.

Mechanical stimuli were applied to a single corpuscle using a blunt glass probe (5 to 10 µm in tip diameter) mounted on a piezoelectric-driven actuator (Physik Instrumente Gmbh). A mechanical step stimulus was applied to corpuscles with variable displacements in increments of 1 µm. The duration of the static and dynamic phases of the step stimulus was constant at 150 and 3 ms, respectively. Vibratory stimuli were applied using a sinusoidal-ramp waveform, increasing 0.25 µm per cycle, at frequencies of 20, 30, 50, 100, 200, and 400 Hz. AP threshold was defined as the smallest probe displacement that elicited an AP. To block APs, 1 µM tetrodotoxin citrate (Tocris) was added to the bath. For experiments with ruptured corpuscles, a puncture was created in the outer core using a high-pressure stream of Krebs solution from a patch pipette.

Patch-clamp electrophysiology

Whole-cell recordings of afferent terminals and LSCs were performed at room temperature, using the same amplifier and digitizer used for single-fiber recording. Borosilicate pipettes with filament and an outer diameter of 1.5 mm, inner diameter of 0.86 mm, wall thickness of 0.32 mm, and tip resistances of 2 to 7 megohms were used to acquire voltage-clamp and current-clamp recordings. Unless otherwise indicated, pipettes were filled with potassium-based internal solution (K-internal) containing 135 mM K-gluconate, 5 mM KCl, 0.5 mM CaCl$_2$, 2 mM MgCl$_2$, 5 mM EGTA, 5 Hepes, 5 mM Na$_2$ATP, and 0.5 mM Na$_2$GTP (pH 7.3 with KOH) and placed on a CV-7B headstage connected to a High-Speed Pressure Clamp. In certain experiments, 1 mM Lucifer yellow (Sigma-Aldrich) was included in the internal solution and fluorescently excited with a U-HGLGPS illumination source (Olympus) and Lucifer yellow filter cube to visualize the patched cell. In all experiments with terminal recordings, Krebs was used as the external bath solution. For patch-clamp recordings from LSCs only, Ringer solution was used as the external solution. Data from intracellular recording were sampled at 20 kHz and low-pass filtered at 2 kHz in Clampex 10.7. Paired recordings from a second cell were acquired with a CV-7B headstage connected to the other channel of the same amplifier and digitizer, using the same single-fiber or patch-clamp techniques described here.

To access the membrane of the afferent terminal and LSCs, a large positive pressure (>100 mmHg) was applied to the recording pipette, which was used to pierce the outer core of the corpuscle and remove obstructions blocking the desired cell. In decapsulation experiments, the inner core was separated entirely from the outer core using this method. Occasionally, multiple patch pipettes were used to blow debris away from the target cell membrane before sealing and break-in. For afferent terminal voltage-clamp recordings, the cells were clamped at −60 mV and the same mechanical stimuli applied during single-fiber recording were used. Only data from healthy terminals (holding currents above −75 pA during voltage-clamp at −60 mV) were used in analysis, except to explore the relationship between the holding current and MA current inactivation rate, in which unhealthy terminals (holding current below −75 pA) were included. The inactivation rate (τ) of the MA current was calculated as described previously (*33*) by fitting a single exponential function [$I = I_0 * \exp(-t/\tau)$, where I_0 is the baseline-subtracted peak current amplitude, t is the time from the peak current, and τ is the inactivation constant] to the decaying portion of the responses in the ON and OFF phases. The MA current threshold was defined as the smallest probe displacement that elicited a response in which the amplitude exceeded 20 pA from baseline.

Electrical properties of LSCs were recorded within 30 s of establishing whole-cell mode. To block gap junctions in certain experiments, 100 µM CBX was included in the internal pipette solution. For paired LSC recording, the coupling coefficient was measured as follows: In current-clamp, a 40- to 100-pA current step was injected into the first cell to elicit a small (< 20 mV) depolarization (V_1). The resultant depolarization in the connected second cell (V_2) was measured, and the ratio V_2/V_1 was calculated. During voltage-clamp experiments, LSCs were clamped at −80 mV unless otherwise

indicated. Mechanical ramp-and-hold stimuli were applied to LSCs with increasing static displacement increments of 0.5 µm held for 150 ms and constant ramp velocities of 1000 µm/s. MA current was recorded with cesium-based intracellular solution (Cs-internal) containing 133 mM CsCl, 10 mM Hepes, 5 mM EGTA, 1 mM CaCl$_2$, 1 mM MgCl$_2$, 4 mM MgATP, and 0.4 mM Na$_2$GTP (pH 7.3 with CsOH). Voltage-gated potassium currents were recorded with K-internal including 100 µM CBX to isolate single LSCs by applying 500-ms depolarizing voltage steps in 20-mV increments (−120 to 120 mV) from −80 mV. Inward Na$^+$/Ca^{2+} voltage-gated currents were recorded using Cs-internal to block potassium current along with 100 µM CBX to isolate single LSCs. In this case, 500-ms depolarizing voltage steps in 20-mV increments (−100 to 120 mV) were applied after hyperpolarizing the cell to −120 mV for 2 s to remove channel inactivation. Voltage-activated conductance was calculated using the equation $G = I/(V_m - E_{rev})$, where G is the conductance, I is the peak current, V_m is the membrane potential, and E_{rev} is the reversal potential. The conductance data were fit with the modified Boltzmann equation $G = G_{min} + (G_{max} - G_{min})/\{1 + \exp([V_{1/2} - V_m]/k)\}$, where G_{min} and G_{max} are the minimal and maximal conductance, respectively, V_m is the voltage, $V_{1/2}$ is the voltage at which the channels reached 50% of their maximal conductance, and k is the slope of the curve. LSC voltage-clamp experiments were corrected offline for liquid junction potential calculated in Clampex 10.7.

Paired recordings were acquired in Krebs solution, with K-internal in patch-clamped cells. Because of the low input resistance of LSCs with open gap junctions, large current injections (1 to 10 nA) were used to generate voltage responses in the inner core capable of depolarizing the afferent in paired recordings. Mechanoreceptor AP threshold in paired single-fiber/LSC patch-clamp recording was measured via 0.010-µm increments from a 0.25-µm range set below and including the baseline threshold determined before the experimental protocol. Two identical mechanical step stimuli of equal displacement were applied, first with the LSC at rest and then with the LSC depolarized by 6 nA for 500 ms starting 150 ms before the second mechanical stimulus. After incrementally increasing the stimulus amplitude, the smallest displacement that elicited an AP with and without LSC activation was defined as the threshold for each condition. Mechanical stimuli were applied to corpuscles before and after experimental protocols to elicit mechanoreceptor APs, confirming health and proper function of the corpuscle and afferent throughout the experiment. All single-fiber and patch-clamp recordings were acquired from corpuscles in skin preparations from at least three different animals. Electrophysiological data were measured in Clampfit 10.7 (Molecular Devices) and then analyzed and displayed in GraphPad Prism 9.5.1 (GraphPad Software LLC).

Enhanced focused ion beam scanning electron microscopy
eFIB-SEM procedures were performed as described previously (27).

Sample preparation
A patch of bill skin was dissected from an E27 duck embryo and immediately immersed into fixative solution containing 2.5% glutaraldehyde, 2.5% paraformaldehyde, 0.13 M cacodylate, 4 mM CaCl$_2$, and 4 mM MgCl$_2$ (pH 7.4, 37°C). The epidermis was removed from the skin, which was then cut into 1 mm–by–1 mm sections at room temperature. The dermis sections were then transferred to fresh fixative solution and gently shaken at 4°C for 48 hours. The solution was replaced with freshly prepared fixative solution at the 24-hour time point. After 48 hours, the sample was stored in a solution of 1.5% paraformaldehyde and 0.13 M cacodylate (pH 7.4) and stored at 4°C.

The bill skin samples were then sectioned into 300-µm-thick slices in 0.13 M cacodylate buffer using a Compresstome (Precisionary, MA). The slices were washed in cacodylate buffer (0.13 M) and postfixed with 2% osmium tetroxide and 1.5% potassium ferrocyanide in 0.13 M cacodylate buffer for 120 min at 0°C. After washing in distilled water, the slices were stained with 1% thiocarbohydrazide for 40 min at 40°C, 2% osmium tetroxide for 90 min at room temperature, followed by 1% uranyl acetate at 4°C overnight. These staining reagents were diluted in the double distilled water. The sample slices were completely washed three times with distilled water between each step at room temperature for 10 min each. Last, the slices were transferred into lead aspartate solution at 50°C for 120 min followed by washing three times with distilled water at room temperature for 10 min each. After the heavy metal staining procedure, the samples were dehydrated with graded ethanol, embedded in Durcupan resin (Sigma-Aldrich, MO), and then polymerized at 60°C for 48 hours.

FIB-SEM sample preparation
Two duck bill skin samples embedded in Durcupan were selected for FIB-SEM sample preparation. The first sample, DB-01MP, included a Pacinian corpuscle in conjunction with a Meissner corpuscle, and the second sample from a different embryo, DB-02P, contained a larger Pacinian corpuscle. Each sample was first mounted on the top of a 1 mm copper post, which was in contact with the metal-stained sample for better charge dissipation, as previously described (79). Each vertical sample post was then trimmed to a small block with a width of 135 µm perpendicular to the ion beam and a depth of 110 µm in the direction of the ion beam sequentially. Both blocks contain the region of interest (ROI) of one complete Pacinian corpuscle. The trimming for DB-01MP was guided by x-ray tomography data from a Zeiss Versa XRM-510, whereas DB-02P's trimming used data from a Zeiss Versa XRM-620, both using a Leica EM UC7 Ultramicrotome for trimming (80).

For conductive coating, a dual layer of 10-nm gold and 100-nm carbon was coated on the DB-01MP using a Gatan 682 High-Resolution Ion Beam Coater. The coating parameters were 6 keV, 200 nA on both argon gas plasma sources, and sample rotation at 10 rpm with 45° tilt. Conversely, DB-02P was first coated with 10-nm gold using a Cressington Sputter Coater 208HR, rotating at 15 rpm with a 30° tilt using a 40-mA argon plasma source, followed by a 40-nm carbon layer deposited using a Leica ACE200 carbon coater.

FIB-SEM 3D large volume imaging
Two FIB-SEM prepared samples, DB-01MP and DB-02P, were imaged using two enhanced FIB-SEM systems, as previously described (79, 81, 82). For DB-01MP, the ROI block face was imaged with a 2-nA electron beam at a 2-MHz scanning rate and a landing energy of 1.2 keV, whereas for DB-02P, it was scanned with a 3-nA electron beam at 3 MHz under the same landing energy condition. Both samples had an x-y pixel size set at 8 nm. A subsequently applied focused Ga$^+$ beam of 15 nA at 30 keV strafed across the top surface and ablated away 8 nm of the surface. The newly exposed surface was then imaged again. The ablation-imaging cycle continued about once every minute for 1 week to complete DB-01MP that contains one Meissner and one Pacinian corpuscle and about once every minute for 2 weeks to complete DB-01P that contains a larger Pacinian

corpuscle from a different embryo. The acquired image stack formed a raw imaged volume, followed by postprocessing of image registration and alignment using a Scale-Invariant Feature Transform–based algorithm. The aligned stack consists of a final isotropic volume of 85 by 56 by 75 μm^3 and 94 by 86 by 120 μm^3 and for DB-01MP and DB-02P, respectively. The voxel size of 8 by 8 by 8 nm^3 was maintained for both samples throughout entire volumes, which can be viewed in any arbitrary orientations.

Electron microscopy segmentation

The segmentation of organelles, cells, and subcellular structures from electron microscopy (EM) images was achieved with ZEISS arivis Cloud, an AI-driven cloud-based platform (https://apeer.com/) (83). Deep learning techniques were used to achieve automated segmentation, using a customized convolutional neural network (CNN) architecture based on 2D U-Net. To generate ground truth data, cells and organelles were manually annotated from a small set (100 planes) of the raw EM images. The CNNs were trained using the annotated ground truth data and proofread to achieve high-quality segmentation of the objects in 3D. Semantic segmentation was applied to each object, and the accuracy of the segmentation was assessed by evaluating the voxel Intersection over Union (IoU) and F1 scores. IoU was calculated as the overlap between annotation and ground truth bounding boxes by computing the ratio of the intersection area to the union area: IoU = (Intersection Area)/(Union Area). The F1 score was calculated as the balance between the model's ability to correctly identify positive samples (precision) and its ability to capture all positive samples (recall): F1 = 2 * (Precision * Recall)/(Precision + Recall) (84). Arivis machine learning models were downloaded separately for each class of cells or organelles to create a full 3D model on a full dataset. All volumes were segmented at 8 nm by 8 nm by 8 nm.

EM reconstruction and data analysis

Raw EM data, along with ZEISS Arivis machine learning models for each class, were imported into the ZEISS Arivis Pro software. This software was used to segment each individual cell and organelle, creating complete objects. In certain cases, ZEISS Arivis Hub from the FIB-SEM Collaboration Core was used to generate the objects. These objects were then filtered by size to eliminate any extraneous noise components. Manual proofreading and adjustments were made as necessary. Various quantitative measures, including volume, distances, surface area, and diameters, were calculated within the software. Videos were generated using Arivis Pro. The 3D TEM tomography was reconstructed at a resolution of 1.6 nm by 1.6 nm by 1.6 nm.

Interactive model of the Pacinian corpuscle in 3D: https://sketchfab.com/3d-models/avian-pacinian-herbst-corpuscle-7b5ab7dc8027406596d5b126bc4f324e

Interactive model of a single LSC in 3D: https://sketchfab.com/3d-models/pacinian-lamellar-schwann-cell-0b42ebddcddd4a489b6842f1a25ed267

3D TEM tomography

Procedures were performed as described previously (27). Freshly peeled duck bill skin was fixed in Karnovsky fixative at 4°C for 1 hour, washed in 0.1 M sodium cacodylate buffer (pH 7.4), and then postfixed in 1% osmium tetroxide for 1 hour in the dark on ice. The tissue was stained in Kellenberger solution for 1 hour at room temperature after washing in distilled water, dehydrated in a series of alcohols and propylene oxide, then embedded in EMbed

812, and polymerized overnight at 60°C. Thick sections of 250 nm in depth were obtained from hardened blocks using a Leica Ultra-Cut UC7 on copper formvar coated slot grids. Sections (250 nm in thickness) were contrast stained using 2% uranyl acetate and lead citrate, and 15 nm of fiducial gold was added to both sides to aid alignment for tomography. Sections were viewed using an FEI Tecnai TF20 at 200 kV, and data were collected using SerialEM (85) at a voxel size of 1.6 by 1.6 by 1.6 nm^3 on an FEI Eagle 4Kx4K charge-coupled device camera using tilt angles of −60 to 60°. All solutions were supplied by Electron Microscopy Sciences (Hatfield, PA).

RNA sequencing of Pacinian inner cores

Single inner cores of Pacinian corpuscles were manually isolated and collected from the ex vivo bill skin preparation under ribonuclease-free conditions for eventual transcriptomic analysis. First, the inner core was separated from the outer core using Krebs-filled patch pipettes with large pressure applied via a High-Speed Pressure Clamp, as described above for electrophysiology. Aspiration pipettes with tip diameters of ~50 to 100 μm filled with 3 μl of RNA Lysis Buffer (Zymo) were then used to aspirate the inner core by applying light negative pressure. The lysis buffer with the inner core from the pipette was then deposited into a 1.5-ml microcentrifuge tube using positive pressure, and 10 μl of extra RNA Lysis Buffer was added to each tube. Samples were then stored at −80°C until RNA isolation. RNA was isolated using the Quick-RNA Microprep Kit (Zymo) per the manufacturer's instructions. RNA concentrations of 113 to 782 pg/μl and RNA Integrity Number (RIN) values in the range of 7.1 to 9.5 were acquired from inner cores, assessed via a 2100 Bioanalyzer (Agilent). RNA from a total of seven inner cores was collected from five independent embryos. RNA was also isolated from six epidermis samples of five separate bill skin preparations as a control.

Library preparation and sequencing were performed by the Yale Center for Genome Analysis. Libraries were prepared using the NEBNext Single Cell/Low Input RNA Library Prep Kit (New England Biolabs), and sequencing was done with an Illumina NovaSeq instrument in the 100–base pair paired-end mode. Approximately 35 million to 87 million sequencing read pairs per sample were obtained. The raw sequencing data were subsequently processed on the Yale Center for Research Computing cluster. First, raw reads were filtered and trimmed using Trimmomatic v0.39 with default parameters. Filtered high-quality reads were then aligned to the duck reference genome using the STAR aligner v2.7.9a with default parameters.

The duck reference genome (https://ftp.ncbi.nlm.nih.gov/genomes/all/GCF/000/355/885/GCF_000355885.1_BGI_duck_1.0/GCF_000355885.1_BGI_duck_1.0_genomic.fna.gz) and gene annotation (https://ftp.ncbi.nlm.nih.gov/genomes/all/GCF/000/355/885/GCF_000355885.1_BGI_duck_1.0/GCF_000355885.1_BGI_duck_1.0_genomic.gff.gz) were obtained from the National Center for Biotechnology Information. The gene annotation was filtered to include only protein-coding genes. Aligned reads were counted by the featureCounts program within the Subread package v2.0.1 with default parameters. Fragments per kilobase of transcript per million mapped reads (FPKM) values were calculated from read counts using the edgeR v3.34.1 package (Bioconductor v3.13) in R v4.1. Statistical analysis of differential expression of genes between groups was evaluated using the Fisher's exact test with the Benjamini-Hochberg method for false discovery in edgeR. RNA sequencing data were deposited to the Gene Expression Omnibus (accession number GSE273272).

To compare the transcriptomic signature of the Pacinian inner core with that of Meissner corpuscles, previously published transcriptomic data from Meissner corpuscles were used (*27*). Transcriptomic data from Pacinian inner core, epidermis, Meissner corpuscles, and bill skin (dermis) were jointly reanalyzed according to the same pipeline described above. Principal components analysis was performed on log-transformed normalized (counts per million) expression data using prcomp function in R. First two principal components were extracted. Group means were determined for the first two principal components. Euclidean distance based on first two principal components between group means was determined using dist function in R.

Supplementary Materials

The PDF file includes:
Figs. S1 to S11
Table S1
Legends for movies S1 and S2
Legend for data S1

Other Supplementary Material for this manuscript includes the following:
Movies S1 and S2
Data S1

REFERENCES AND NOTES

1. A. Handler, D. D. Ginty, The mechanosensory neurons of touch and their mechanisms of activation. *Nat. Rev. Neurosci.* **22**, 521–537 (2021).
2. E. R. Schneider, E. O. Gracheva, S. N. Bagriantsev, Evolutionary specialization of tactile perception in vertebrates. *Phys. Ther.* **31**, 193–200 (2016).
3. L. H. Ziolkowski, E. O. Gracheva, S. N. Bagriantsev, Tactile sensation in birds: Physiological insights from avian mechanoreceptors. *Curr. Opin. Neurobiol.* **74**, 102548 (2022).
4. R. Cobo, J. Garcia-Piqueras, J. Cobo, J. A. Vega, The human cutaneous sensory corpuscles: An update. *J. Clin. Med.* **10**, 227 (2021).
5. W. H. Talbot, I. Darian-Smith, H. H. Kornhuber, V. B. Mountcastle, The sense of flutter-vibration: Comparison of the human capacity with response patterns of mechanoreceptive afferents from the monkey hand. *J. Neurophysiol.* **31**, 301–334 (1968).
6. K. M. Gottschaldt, The physiological basis of tactile sensibility in the beak of geese. *J. Comp. Physiol.* **95**, 29–47 (1974).
7. K. S. Lee, A. J. Loutit, D. de Thomas Wagner, M. Sanders, M. Prsa, D. Huber, Transformation of neural coding for vibrotactile stimuli along the ascending somatosensory pathway. *Neuron* **112**, 3343–3353.e7 (2024).
8. J. Turecek, D. D. Ginty, Coding of self and environment by Pacinian neurons in freely moving animals. *Neuron* **112**, 3267–3277.e6 (2024).
9. K. S. Lee, A. J. Loutit, D. de Thomas Wagner, M. Sanders, D. Huber, Emergence of a brainstem somatosensory tonotopic map for substrate vibration. *Nat. Neurosci.* **28**, 97–104 (2024).
10. S. J. Bolanowski Jr., J. J. Zwislocki, Intensity and frequency characteristics of Pacinian corpuscles. I. Action potentials. *J. Neurophysiol.* **51**, 793–811 (1984).
11. J. Bell, S. Bolanowski, M. H. Holmes, The structure and function of Pacinian corpuscles: A review. *Prog. Neurobiol.* **42**, 79–128 (1994).
12. R. Saxod, Ontogeny of the cutaneous sensory organs. *Microsc. Res. Tech.* **34**, 313–333 (1996).
13. J. Zelena, Z. Halata, V. Szeder, M. Grim, Crural Herbst corpuscles in chicken and quail: Numbers and structure. *Anat. Embryol.* **196**, 323–333 (1997).
14. S. J. Bolanowski, J. E. Schyuler, N. B. Slepecky, Semi-serial electron-micrographic reconstruction of putative transducer sites in Pacinian corpuscles. *Somatosens. Mot. Res.* **11**, 205–218 (1994).
15. A. Handler, Q. Zhang, S. Pang, T. M. Nguyen, M. Iskols, M. Nolan-Tamariz, S. Cattel, R. Plumb, B. Sanchez, K. Ashjian, A. Shotland, B. Brown, M. Kabeer, J. Turecek, M. M. DeLisle, G. Rankin, W. Xiang, E. C. Pavarino, N. Africawala, C. Santiago, W. A. Lee, C. S. Xu, D. D. Ginty, Three-dimensional reconstructions of mechanosensory end organs suggest a unifying mechanism underlying dynamic, light touch. *Neuron* **111**, 3211–3229.e9 (2023).
16. P. K. Dorward, A. K. McIntyre, Responses of vibration-sensitive receptors in the interosseous region of the duck's hind limb. *J. Physiol.* **219**, 77–87 (1971).
17. I. Suazo, J. A. Vega, Y. Garcia-Mesa, J. Garcia-Piqueras, O. Garcia-Suarez, T. Cobo, The lamellar cells of vertebrate Meissner and Pacinian corpuscles: Development, characterization, and functions. *Front. Neurosci.* **16**, 790130 (2022).
18. W. R. Loewenstein, R. Skalak, Mechanical transmission in a Pacinian corpuscle. An analysis and a theory. *J. Physiol.* **182**, 346–378 (1966).
19. J. C. Quindlen, H. K. Stolarski, M. D. Johnson, V. H. Barocas, A multiphysics model of the Pacinian corpuscle. *Integr. Biol. (Camb)* **8**, 1111–1125 (2016).
20. J. C. Quindlen-Hotek, E. T. Bloom, O. K. Johnston, V. H. Barocas, An inter-species computational analysis of vibrotactile sensitivity in Pacinian and Herbst corpuscles. *R. Soc. Open Sci.* **7**, 191439 (2020).
21. D. R. Logan, J. Hall, L. Bianchi, A helping hand: Roles for accessory cells in the sense of touch across species. *Front. Cell. Neurosci.* **18**, 1367476 (2024).
22. L. Pawson, L. T. Prestia, G. K. Mahoney, B. Guclu, P. J. Cox, A. K. Pack, GABAergic/glutamatergic-glial/neuronal interaction contributes to rapid adaptation in Pacinian corpuscles. *J. Neurosci.* **29**, 2695–2705 (2009).
23. S. Meltzer, K. C. Boulanger, E. Osei-Asante, A. Handler, Q. Zhang, C. Sano, S. Itohara, D. D. Ginty, A role for axon-glial interactions and Netrin-G1 signaling in the formation of low-threshold mechanoreceptor end organs. *Proc. Natl. Acad. Sci. U.S.A.* **119**, e2210421119 (2022).
24. W. R. Loewenstein, M. Mendelson, Components of receptor adaptation in a Pacinian corpuscle. *J. Physiol.* **177**, 377–397 (1965).
25. M. Mendelson, W. R. Loewenstein, Mechanisms of receptor adaptation. *Science* **144**, 554–555 (1964).
26. R. Saxod, "Development of cutaneous sensory receptors in birds" in *Development of Sensory System*, C. M. Bate, Ed. (Springer-Verlag, 1978), chap. 8, pp. 337–417.
27. Y. A. Nikolaev, L. H. Ziolkowski, S. Pang, W.-P. Li, V. V. Feketa, C. S. Xu, E. O. Gracheva, S. N. Bagriantsev, 3D architecture and a bicellular mechanism of touch detection in mechanosensory corpuscle. *Sci. Adv.* **9**, eadi4147 (2023).
28. L. H. Ziolkowski, E. O. Gracheva, S. N. Bagriantsev, Mechanotransduction events at the physiological site of touch detection. *eLife* **12**, e84179 (2023).
29. J. A. Gray, M. Sato, The movement of sodium and other ions in Pacinian corpuscles. *J. Physiol.* **129**, 594–607 (1955).
30. O. B. Ilyinsky, G. N. Akoev, T. L. Krasnikova, S. I. Elman, K and Na ion content in the Pacinian corpuscle fluid and its role in the activity of receptors. *Pflugers Arch.* **361**, 279–285 (1976).
31. H. Berkhoudt, The morphology and distribution of cutaneous mechanoreceptors (Herbst and Grandry corpuscles) in bill and tongue of the Mallard (Anas platyrhynchos L.). *Neth. J. Zool.* **30**, 1–34 (1980).
32. D. C. Pease, T. A. Quilliam, Electron microscopy of the Pacinian corpuscle. *J. Biophys. Biochem. Cytol.* **3**, 331–342 (1957).
33. Y. A. Nikolaev, V. V. Feketa, E. O. Anderson, E. R. Schneider, E. O. Gracheva, S. N. Bagriantsev, Lamellar cells in Pacinian and Meissner corpuscles are touch sensors. *Sci. Adv.* **6**, eabe6393 (2020).
34. Z. Zhou, X. Ma, Y. Lin, D. Cheng, N. Bavi, G. A. Secker, J. V. Li, V. Janbandhu, D. L. Sutton, H. S. Scott, M. Yao, R. P. Harvey, N. L. Harvey, B. Corry, Y. Zhang, C. D. Cox, MyoD-family inhibitor proteins act as auxiliary subunits of Piezo channels. *Science* **381**, 799–804 (2023).
35. R. Syeda, Physiology and pathophysiology of mechanically activated PIEZO channels. *Annu. Rev. Neurosci.* **44**, 383–402 (2021).
36. J. M. Kefauver, A. B. Ward, A. Patapoutian, Discoveries in structure and physiology of mechanically activated ion channels. *Nature* **587**, 567–576 (2020).
37. W. A. Catterall, Voltage gated sodium and calcium channels: Discovery, structure, function, and Pharmacology. *Channels (Austin)* **17**, 2281714 (2023).
38. Y.-T. Chen, D. de Thomas Wagner, A. J. Loutit, A. Nourizonoz, M.-C. Croisier-Coeytaux, J. Blanc, G. Knott, K.-S. Lee, D. Huber, Lamellar Schwann cells in the Pacinian corpuscle potentiate vibration perception. bioRxiv 2024.2008.2023.609459 [Preprint] (2024). https://doi.org/10.1101/2024.08.23.609459.
39. W. R. Loewenstein, R. Rathkamp, The sites for mechano-electric conversion in a Pacinian corpuscle. *J. Gen. Physiol.* **41**, 1245–1265 (1958).
40. W. R. Loewenstein, R. Rathkamp, Localization of generator structures of electric activity in a Pacinian corpuscle. *Science* **127**, 341 (1958).
41. M. Ozeki, M. Sato, Changes in the membrane potential and the membrane conductance associated with a sustained compression of the non-myelinated nerve terminal in Pacinian corpuscles. *J. Physiol.* **180**, 186–208 (1965).
42. C. C. Hunt, A. Takeuchi, Responses of the nerve terminal of the Pacinian corpuscle. *J. Physiol.* **160**, 1–21 (1962).
43. K. Nishi, M. Sato, Depolarizing and hyperpolarizing receptor potentials in the non-myelinated nerve terminal in Pacinian corpuscles. *J. Physiol.* **199**, 383–396 (1968).
44. R. O'Hagan, M. Chalfie, M. B. Goodman, The MEC-4 DEG/ENaC channel of Caenorhabditis elegans touch receptor neurons transduces mechanical signals. *Nat. Neurosci.* **8**, 43–50 (2005).
45. S. Katta, A. Sanzeni, A. Das, M. Vergassola, M. B. Goodman, Progressive recruitment of distal MEC-4 channels determines touch response strength in C. elegans. *J. Gen. Physiol.* **151**, 1213–1230 (2019).
46. A. L. Eastwood, A. Sanzeni, B. C. Petzold, S. J. Park, M. Vergassola, B. L. Pruitt, M. B. Goodman, Tissue mechanics govern the rapidly adapting and symmetrical response to touch. *Proc. Natl. Acad. Sci. U.S.A.* **112**, E6955–E6963 (2015).
47. A. Das, J. A. Franco, B. Mulcahy, L. Wang, D. Chapman, C. Jaisinghani, B. L. Pruitt, M. Zhen, M. B. Goodman, *C. elegans* touch receptor neurons direct mechanosensory complex

organization via repurposing conserved basal lamina proteins. *Curr. Biol.* **34**, 3133–3151.e10 (2024).

48. A. Yamada, J. Ling, A. I. Yamada, H. Furue, J. G. Gu, ASICs mediate fast excitatory synaptic transmission for tactile discrimination. *Neuron* **112**, 1286–1301.e8 (2024).

49. Y. Garcia-Mesa, J. Feito, P. Cuendias, J. Garcia-Piqueras, A. Germana, O. Garcia-Suarez, B. Martin-Biedma, J. A. Vega, The acquisition of mechanoreceptive competence by human digital Merkel cells and sensory corpuscles during development: An immunohistochemical study of PIEZO2. *Ann. Anat.* **243**, 151953 (2022).

50. S. S. Ranade, S. H. Woo, A. E. Dubin, R. A. Moshourab, C. Wetzel, M. Petrus, J. Mathur, V. Begay, B. Coste, J. Mainquist, A. J. Wilson, A. G. Francisco, K. Reddy, Z. Qiu, J. N. Wood, G. R. Lewin, A. Patapoutian, Piezo2 is the major transducer of mechanical forces for touch sensation in mice. *Nature* **516**, 121–125 (2014).

51. Y. Garcia-Mesa, P. Cuendias, M. Alonso-Guervos, J. Garcia-Piqueras, B. Martin-Biedma, T. Cobo, O. Garcia-Suarez, J. A. Vega, Immunohistochemical detection of PIEZO1 and PIEZO2 in human digital Meissner's corpuscles. *Ann. Anat.* **252**, 152200 (2024).

52. E. R. Schneider, E. O. Anderson, V. V. Feketa, M. Mastrotto, Y. A. Nikolaev, E. O. Gracheva, S. N. Bagriantsev, A cross-species analysis reveals a general role for piezo2 in mechanosensory specialization of trigeminal ganglia from tactile specialist birds. *Cell Rep.* **26**, 1979–1987.e3 (2019).

53. E. R. Schneider, M. Mastrotto, W. J. Laursen, V. P. Schulz, J. B. Goodman, O. H. Funk, P. G. Gallagher, E. O. Gracheva, S. N. Bagriantsev, Neuronal mechanism for acute mechanosensitivity in tactile-foraging waterfowl. *Proc. Natl. Acad. Sci. U.S.A.* **111**, 14941–14946 (2014).

54. E. R. Schneider, E. O. Anderson, M. Mastrotto, J. D. Matson, V. P. Schulz, P. G. Gallagher, R. H. LaMotte, E. O. Gracheva, S. N. Bagriantsev, Molecular basis of tactile specialization in the duck bill. *Proc. Natl. Acad. Sci. U.S.A.* **114**, 13036–13041 (2017).

55. B. Coste, J. Mathur, M. Schmidt, T. J. Earley, S. Ranade, M. J. Petrus, A. E. Dubin, A. Patapoutian, Piezo1 and Piezo2 are essential components of distinct mechanically activated cation channels. *Science* **330**, 55–60 (2010).

56. E. O. Anderson, E. R. Schneider, J. D. Matson, E. O. Gracheva, S. N. Bagriantsev, TMEM150C/Tentonin3 is a regulator of mechano-gated ion channels. *Cell Rep.* **23**, 701–708 (2018).

57. X. Zhang, J. Shao, C. Wang, C. Liu, H. Hao, X. Li, Y. An, J. He, W. Zhao, Y. Zhao, Y. Kong, Z. Jia, S. Wan, Y. Yuan, H. Zhang, H. Zhang, X. Du, TMC7 functions as a suppressor of Piezo2 in primary sensory neurons blunting peripheral mechanotransduction. *Cell Rep.* **43**, 114014 (2024).

58. J. S. Del Rosario, M. Gabrielle, Y. Yudin, T. Rohacs, TMEM120A/TACAN inhibits mechanically activated PIEZO2 channels. *J. Gen. Physiol.* **154**, e202213164 (2022).

59. A. E. Dubin, M. Schmidt, J. Mathur, M. J. Petrus, B. Xiao, B. Coste, A. Patapoutian, Inflammatory signals enhance piezo2-mediated mechanosensitive currents. *Cell Rep.* **2**, 511–517 (2012).

60. I. Schaefer, C. Verkest, L. Vespermann, T. Mair, H. Voss, N. Zeitzschel, S. G. Lechner, PKA mediates modality-specific modulation of the mechanically gated ion channel PIEZO2. *J. Biol. Chem.* **299**, 104782 (2023).

61. L. O. Romero, R. Caires, A. Kaitlyn Victor, J. Ramirez, F. J. Sierra-Valdez, P. Walsh, V. Truong, J. Lee, U. Mayor, L. T. Reiter, V. Vasquez, J. F. Cordero-Morales, Linoleic acid improves PIEZO2 dysfunction in a mouse model of Angelman Syndrome. *Nat. Commun.* **14**, 1167 (2023).

62. W. Zheng, Y. A. Nikolaev, E. O. Gracheva, S. N. Bagriantsev, Piezo2 integrates mechanical and thermal cues in vertebrate mechanoreceptors. *Proc. Natl. Acad. Sci. U.S.A.* **116**, 17547–17555 (2019).

63. S. Ma, A. E. Dubin, L. O. Romero, M. Loud, A. Salazar, S. Chu, N. Klier, S. Masri, Y. Zhang, Y. Wang, A. T. Chesler, K. A. Wilkinson, V. Vasquez, K. L. Marshall, A. Patapoutian, Excessive mechanotransduction in sensory neurons causes joint contractures. *Science* **379**, 201–206 (2023).

64. L. O. Romero, R. Caires, A. R. Nickolls, A. T. Chesler, J. F. Cordero-Morales, V. Vasquez, A dietary fatty acid counteracts neuronal mechanical sensitization. *Nat. Commun.* **11**, 2997 (2020).

65. W. Zheng, E. O. Gracheva, S. N. Bagriantsev, A hydrophobic gate in the inner pore helix is the major determinant of inactivation in mechanosensitive Piezo channels. *eLife* **8**, e44003 (2019).

66. N. Zeitzschel, S. G. Lechner, The activation thresholds and inactivation kinetics of poking-evoked PIEZO1 and PIEZO2 currents are sensitive to subtle variations in mechanical stimulation parameters. *Channels (Austin)* **18**, 2355123 (2024).

67. B. U. Hoffman, Y. Baba, T. N. Griffith, E. V. Mosharov, S. H. Woo, D. D. Roybal, G. Karsenty, A. Patapoutian, D. Sulzer, E. A. Lumpkin, Merkel cells activate sensory neural pathways through adrenergic synapses. *Neuron* **100**, 1401–1413.e6 (2018).

68. W. Chang, H. Kanda, R. Ikeda, J. Ling, J. J. DeBerry, J. G. Gu, Merkel disc is a serotonergic synapse in the epidermis for transmitting tactile signals in mammals. *Proc. Natl. Acad. Sci. U.S.A.* **113**, E5491–E5500 (2016).

69. B. Graziano, L. Wang, O. R. White, D. H. Kaplan, J. Fernandez-Abascal, L. Bianchi, Glial KCNQ K+ channels control neuronal output by regulating GABA release from glia in *C. elegans*. *Neuron* **112**, 1832–1847.e7 (2024).

70. J. Fernandez-Abascal, C. K. Johnson, B. Graziano, L. Wang, N. Encalada, L. Bianchi, A glial ClC Cl− channel mediates nose touch responses in *C. elegans*. *Neuron* **110**, 470–485.e7 (2022).

71. F. Moehring, A. M. Cowie, A. D. Menzel, A. D. Weyer, M. Grzybowski, T. Arzua, A. M. Geurts, O. Palygin, C. L. Stucky, Keratinocytes mediate innocuous and noxious touch via ATP-P2X4 signaling. *eLife* **7**, e31684 (2018).

72. M. Beurg, X. Tan, R. Fettiplace, A prestin motor in chicken auditory hair cells: Active force generation in a nonmammalian species. *Neuron* **79**, 69–81 (2013).

73. J. Hu, L. Y. Chiang, M. Koch, G. R. Lewin, Evidence for a protein tether involved in somatic touch. *EMBO J.* **29**, 855–867 (2010).

74. L. Li, D. D. Ginty, The structure and organization of lanceolate mechanosensory complexes at mouse hair follicles. *eLife* **3**, e01901 (2014).

75. F. Schwaller, V. Begay, G. Garcia-Garcia, F. J. Taberner, R. Moshourab, B. McDonald, T. Docter, J. Kuhnemund, J. Ojeda-Alonso, R. Paricio-Montesinos, S. G. Lechner, J. F. A. Poulet, J. M. Millan, G. R. Lewin, USH2A is a Meissner's corpuscle protein necessary for normal vibration sensing in mice and humans. *Nat. Neurosci.* **24**, 74–81 (2021).

76. J. Ojeda-Alonso, L. Calvo-Enrique, R. Paricio-Montesinos, R. Kumar, M. D. Zhang, J. F. A. Poulet, P. Ernfors, G. R. Lewin, Sensory Schwann cells set perceptual thresholds for touch and selectively regulate mechanical nociception. *Nat. Commun.* **15**, 898 (2024).

77. H. Abdo, L. Calvo-Enrique, J. M. Lopez, J. Song, M. D. Zhang, D. Usoskin, A. El Manira, I. Adameyko, H. Hjerling-Leffler, P. Ernfors, Specialized cutaneous Schwann cells initiate pain sensation. *Science* **365**, 695–699 (2019).

78. L. Qi, M. Iskols, R. S. Greenberg, J. Y. Xiao, A. Handler, S. D. Liberles, D. D. Ginty, Krause corpuscles are genital vibrotactile sensors for sexual behaviours. *Nature* **630**, 926–934 (2024).

79. C. S. Xu, K. J. Hayworth, Z. Lu, P. Grob, A. M. Hassan, J. G. Garcia-Cerdan, K. K. Niyogi, E. Nogales, R. J. Weinberg, H. F. Hess, Enhanced FIB-SEM systems for large-volume 3D imaging. *eLife* **6**, e25916 (2017).

80. S. Pang, C. S. Xu, Chapter 11—Methods of enhanced FIB-SEM sample preparation and image acquisition. *Methods Cell Biol.* **177**, 269–300 (2023).

81. C. S. Xu, S. Pang, K. J. Hayworth, H. F. Hess, "Transforming FIB-SEM systems for large-volume connectomics and cell biology" in *Volume Microscopy: Multiscale Imaging with Photons, Electrons, and Ions*, I. Wacker, E. Hummel, S. Burgold, R. Schröder, Eds. (Springer US, 2020), pp. 221–243.

82. C. S. Xu, S. Pang, G. Shtengel, A. Muller, A. T. Ritter, H. K. Hoffman, S. Y. Takemura, Z. Lu, H. A. Pasolli, N. Iyer, J. Chung, D. Bennett, A. V. Weigel, M. Freeman, S. B. van Engelenburg, T. C. Walther, R. V. Farese Jr., J. Lippincott-Schwartz, I. Mellman, M. Solimena, H. F. Hess, An open-access volume electron microscopy atlas of whole cells and tissues. *Nature* **599**, 147–151 (2021).

83. D. Dang, M. Le, T. Irmer, O. Angay, B. Fichtl, B. Schwarz, APEER: An Interactive Cloud Platform for Microscopists to Easily Deploy Deep Learning (Zenodo, 2021).

84. R. Padilla, S. L. Netto, E. A. B. da Silva, in *2020 International Conference on Systems, Signals and Image Processing (IWSSIP)* (IEEE, 2020), pp. 237–242.

85. D. N. Mastronarde, Automated electron microscope tomography using robust prediction of specimen movements. *J. Struct. Biol.* **152**, 36–51 (2005).